Qufei Li, Sherry Wanderling, Marcin Paduch, David Medovoy, Abhishek Singharoy, Ryan McGreevy, Carlos Villalba-Galea, Raymond Hulse, Benoit Roux, Klaus Schulten, Anthony Kossiakoff and Eduardo Perozo

Structural Mechanism of Voltage-Dependent Gating in an Isolated Voltage-Sensing Domain

*To whom correspondence should be addressed. E-mail: eperozo@uchicago.edu

Supplementary Information:

Extended methods and procedures
Figures S1-S6
References

EXTENDED METHODS AND PROCEDURES

Data collection. All data were collected at the Advanced Photon Source synchrotron (beamlines 24-ID-E, 24-ID-C, 23-ID-B or 23-ID-D) under a nitrogen stream at 100 K, and processed with HKL2000. For the Ci-VSD-R217E+33F12_4 complex crystals, single rod (needle) shaped crystal (~20 µm X 30 µm X 100 µm dimension) produced the complete data set by continuous vector-scan collection with a 20 µm micro-focused beam. For the Ci-VSD-WT+39D10_18 complex, P1 space group crystals contained multiple lattices. Due to the small size (~10 µm X 40 µm X 50 µm dimension) and weak diffraction of the crystals, data had to be collected without attenuation for at least 2 seconds exposure per frame to obtain the highest resolution. Only partial datasets (20~60% completeness) could be collected from single crystals due to severe radiation damage. Overall, 40 fractional data sets around 3.6 – 4.5 Å were collected and processed from > 1000 screened crystals. From these, a total of 8 fractional data sets were compatibly merged into a nominal 3.8 Å data set. The unit cell dimensions and angles for the merged data set were adjusted to the average values from the 8 individual sets with ~1.5 Å deviation on dimensions and ~1^{o} on angles.

Structure determination. The final Ci-VSD R217E structures were refined to R_{work}/R_{free} = 0.173/0.236 (for 2.5 Å data set) and R_{work}/R_{free} = 0.173/0.261 (for 2.8 Å data set) containing residues 101-236 for Ci-VSD R217E. The side chains are well resolved throughout Ci-VSD R217E+33F12_4 complex including the voltage sensor as shown by the $2F_o$-F_c electron density map at 2.5 Å resolution (Figure S1B).

Phases for the Ci-VSD WT+39D10_18 complex data were determined by molecular replacement using the Fab and Ci-VSD R217E as search models. As the electron density improved after iterative adjustment and refinement, significant differences between the Ci-VSD WT electron density map and the search model became evident. Starting from residues 200 in the S3-S4 loop (Figure S5A), these discrepancies could not be matched by simple backbone adjustment, and as a consequence, all residues from the loop to the end of protein were trimmed and rebuilt. Several obvious electron density “knobs” helped position a series of adjacent bulky residues (F199, Y200, E205 and R223, Figure S5A). Aided by density modification and B-factor sharpening (DeLaBarre and Brunger, 2006), the WT model was built to residue 244, the last amino acid of the construct used for crystallization. This density extends considerably beyond the last visible residue in Ci-VSD R217E structure (residue 236), forms a short helix that represents the linker between the VSD and the phosphatase domains. Four fold NCS with strict backbone and moderate side chain was imposed separately on the three individual domains: Ci-VSD WT, the variable domain of Fab and the constant domain of Fab. The WT model was refined to R_{work}/R_{free} = 0.248/0.292 including data to 3.6 Å resolution (I/σ = 1.0 with 83% completeness at highest shell). Stringent geometric constrain on bond length and angle were imposed at last stage of refinement to improve the quality of the structural model.

In the Down conformation sensor structure, there are four Ci-VSD WT+39D10_18 complexes in the asymmetric unit of P1 space group. The major differences among the four copies result from the flexibility between the individual domains (up to 12 Å deviation at constant domain of the Fab when aligned at Ci-VSD-WT, Figure S3D right). The constant and variable domains of the Fab are essential identical (Figure S3D left).

The four copies of the Ci-VSD WT are also identical, except for the inter-domain S4-phosphatase linker, where it is present in only three out of four copies (Figure S3E). This heterogeneity suggests an intrinsic structural diversity of the linker region, since the S4 in all four Ci-VSD WT copies experience the same dimer interface interactions in the crystal lattice. In contrast, no linker is visible at even higher resolution (2.5 Å) in the Ci-VSD R217E structure. This comparison points to the intrinsic dynamics of the inter-domain linker, that it is relatively more stable in the down state in Ci-VSD WT than the up state in Ci-VSD R217E.

S4 position in low resolution crystallographic data by molecular dynamics flexible fitting. A novel computational approach, termed xMDFF, for reconstructing all-atom structures from low resolution X-ray diffraction data is briefly discussed. xMDFF is derived from the Molecular Dynamics Flexible Fitting (MDFF) method which solves atomic models of biomolecules imaged by cryo-electron microscopy. In the MDFF method, an initial atomic model is subjected to a molecular dynamics (MD) simulation with a modified potential energy function that includes a term derived from the cryo-EM density map (Trabuco et al., 2008; Trabuco et al., 2009). Through the density-dependent term, atoms experience steering forces, f^{fit}, that locally drive them toward high-density regions, thereby fitting the atoms to the map. For use with low resolution X-ray crystallography, the MDFF protocol is modified to work with densities derived from molecular replacement which uses the phases ϕ from a tentative model and the amplitudes $|F|$ from the X-ray diffraction data (Figure S4A, S4B). The densities are 2mFo-DFc maps created using the Phenix software suite (Adams et al., 2010). Next, the tentative model is flexibly fitted into the electron density map using MDFF. In addition to the steering forces derived from the density data, structural restraints are applied to preserve secondary structure of proteins and nucleic acids (Trabuco et al., 2008; Trabuco et al., 2009), as well as to ensure stereochemical correctness (Schreiner et al., 2011), thus avoiding over-fitting the model into the map. Using phases from the fitted structure and experimental diffraction amplitudes, the electron density is regenerated. The MDFF-fitted structure is then used as an updated model to be fitted to the new map. This way, given X-ray diffraction amplitude, calculations for updating the electron density map and generating the atomic model will iteratively refine the unknown phase angles. Phase improvement is indicated by a decrease in R-factors with subsequent iterations. The iterations continue until the R-free/work reaches a minimum or becomes lower than a predefined tolerance. The xMDFF methodology has been tested for six low-resolution (4-4.5 Å) protein structures of varying sizes as presented in Figure S4C. An improvement in the R-free and R-work over and above those reported experimentally is observed in almost all the cases. Furthermore, consistently low Molprobity (Chen et al., 2010) scores and close R-free and R-work values suggest minimal over-fitting in the predicted all-atom geometries. Next, xMDFF was applied to solve the structure of Ci-VSD using 3.6 and 4 Å data. Refinement started from a medium-confidence homology model developed with information from thirteen proteins. During refinement, the tentative model underwent a remarkable large-scale deformation with an RMSD of 5 Å. Unlike many traditional refinement techniques, xMDFF is able to handle these large-scale structural deformations between the initial and final structures, producing a final R-free of 0.27 starting from the initial 0.46. Positioning of the S4

helices is in excellent agreement with the WT structure independently predicted from experiments, with an RMSD ranging from 0.4-1 Å.

Additional electron-marker strategies in the Ci-VSD-WT complex. In an attempt to improve the diffracting properties of the Ci-VSD-WT crystals we carried out a sustained and extensive exploration of additional conditions, including different antibodies, various truncations on Ci-VSD, further detergent and additive screening. These attempts proved unsuccessful in improving the resolution of the Ci-VSD-WT data past 3.6 Å. Subsequently, we focused our efforts to place an electron density marker on the S4 of Ci-VSD-WT as a way to additionally confirm the S4 helix position. The approaches were carried out through either mercuric compound labeling on engineered cysteine residues or Se-Met incorporation through engineered methionines.

For mercury modification, two extra single cysteines were introduced at positions 218 and 228 on Ci-VSD-WT-106-244. These single cysteine Ci-VSD mutants generated similar crystals as native WT. Four mercury-containing compounds (mercury (II) chloride, methyl mercury chloride, ethyl mercury chloride and p-chloromercuribenzoic acid) were added to Ci-VSD cysteine mutant at various stages of the crystallization process: before complex with antibody, co-crystallization, soaking or application of labeling powder directly onto the crystal drop. 5 min soaking with 1 mM mercury (II) chloride severely compromised diffraction properties without any noticeable changes on crystal size or shape. We were able to obtain several data sets (4.1-4.5 Å) by co-crystallization with up to 2 mM methyl mercury and ethyl mercury. However, we found no Hg signal on either difference or anomalous maps. Co-crystallization at higher mercury concentrations (> 5 mM) failed to produce crystals. Ci-VSD single cysteine mutants were also modified by mercury-containing compounds and purified before forming the antibody complex. The resulting crystals were much smaller than native crystals and never diffracted better than 5 Å. We were able to collect a 6.5 Å data at 85% completeness from single crystal. Even though the X-ray fluorescence confirmed the existence of mercury in the crystal, no mercury signal was present in either the difference or anomalous map. These data point to an intrinsic inability to generate Ci-VSD-WT diffracting crystals in the presence of a wide range of mercury modifications.

As an alternative, two additional single methionines were introduced at positions 218 and 228 on Ci-VSD-WT-106-244 for Se-Met incorporation. The crystals from methionine mutants with 39D10_18 Fab were smaller and softer than native WT crystals, and were stable for only 4~5 days and gradually faded away. Nevertheless, significant X-ray fluorescence and edge scan confirmed successful selenium incorporation in the crystals. Inconveniently, they diffract far worse than the native crystals. After screening ~300 Se-Met crystals, we managed to collect at best, a 7 Å data set from Ci-VSD-218M + 39D10_18 complex with 80% completeness, and its anomalous map only contain one confident methionine M133 on S chain among 28 potential sites within four copies of complex in whole ASU. We attempted to improve the anomalous data by merging different data sets with significantly improved statistics (including completeness, resolution, I/σ) and satisfactory Rmerge, but the resulting electron density map ($2F_o$-F_c) was always worse than the starting partial data. Direct comparison of asymmetric units of four partial low resolution (6.5~7.5 Å) data sets revealed considerable crystal heterogeneity. Within ~2% variation on cell dimensions and angles of the P1 space

group, the protein backbone could deviate up to 7 Å among the different models, a fact that explains our inability to merge low resolution data. Since the Se-Met incorporated crystals diffracted only to 5~6 Å and the heterogeneity of the crystals at low resolution prohibited data merging, the only possibility of success relied on the use of single Se-Met crystals to collect complete data, a condition that was not achieved even when using standard WT crystals.

Given our unsuccessful attempts to carry out an electron-marker strategy with both mercuric compound modification and Se-Met incorporation, it is reasonable to believe that we have explored the limit of from this Ci-VSD-WT+39D10_18 complex crystals in different ways. This suggests that the quest for higher resolution Ci-VSD-WT data will probably require s restart of our entire crystallization approach.

Molecular dynamic simulations. A total of four all-atom molecular models of the Ci-VSP voltage sensor were built in an explicit POPC membrane environment using CHARMM-GUI (Jo et al., 2008): one of the down state (WT), one of the up state (R271E), and one of each of those two states with only those residues (residues 106-236) resolved in both crystal structures. The two "overlap" structures were precisely identical in atomistic composition. In both up-state systems, the R217E mutation was reversed *in silico*. Proteins were initially placed in the membrane following established positioning for the up (Khalili-Araghi et al., 2010) and the down states (Vargas et al., 2011) of the voltage sensor. The CHARMM36 parameter set (Klauda et al., 2010) was used for lipids, CHARMM22 with CMAP corrections for protein (MacKerell et al., 1998), and the TIP3P (Jorgensen et al., 1983) model for waters. Total system size in each case was ~63-72k atoms including 150mM KCl. Each of these four systems was run for 20 ns of Molecular Dynamics at 315°K using the program NAMD (Phillips et al., 2005), with 2 fs time steps, periodic boundary conditions, particle-mesh Ewald electrostatics, and a 12 Å real-space cutoff. The full-length WT structure was run for a total 105ns, using ANTON (Shaw et al., 2008), and the full-length Up-state model for a total of 60ns. Additionally, for both of the "overlap" structures, another 20 ns was performed for applied transmembrane voltages of +100 mV, 0 mV and -100 mV. Also, for the down-state system, another 95 ns of simulation was performed on ANTON (Shaw et al., 2008), with the CHARMM27 force field for lipids (Feller and MacKerell, 2000).

Since the shortened up-state model and the down-state model represent different configurations of an identical atomistic system, they can be used to compute a gating charge (Roux, 2008). Gating charge calculations were done using the last 15ns of each 20ns simulation, for -100 mV, 0 mV, and +100 mV. To look at the interactions between ARG residues on S4 and their counter-charges, the NAMD energy plug-in of the program VMD (Humphrey et al., 1996) was used to compute the electrostatic interaction energies between residues, using the CHARMM force field, for each frame of the Molecular Dynamics trajectories – the 95 ns of ANTON trajectory for the down state, and the second half of the 10 ns trajectory for the full up state.

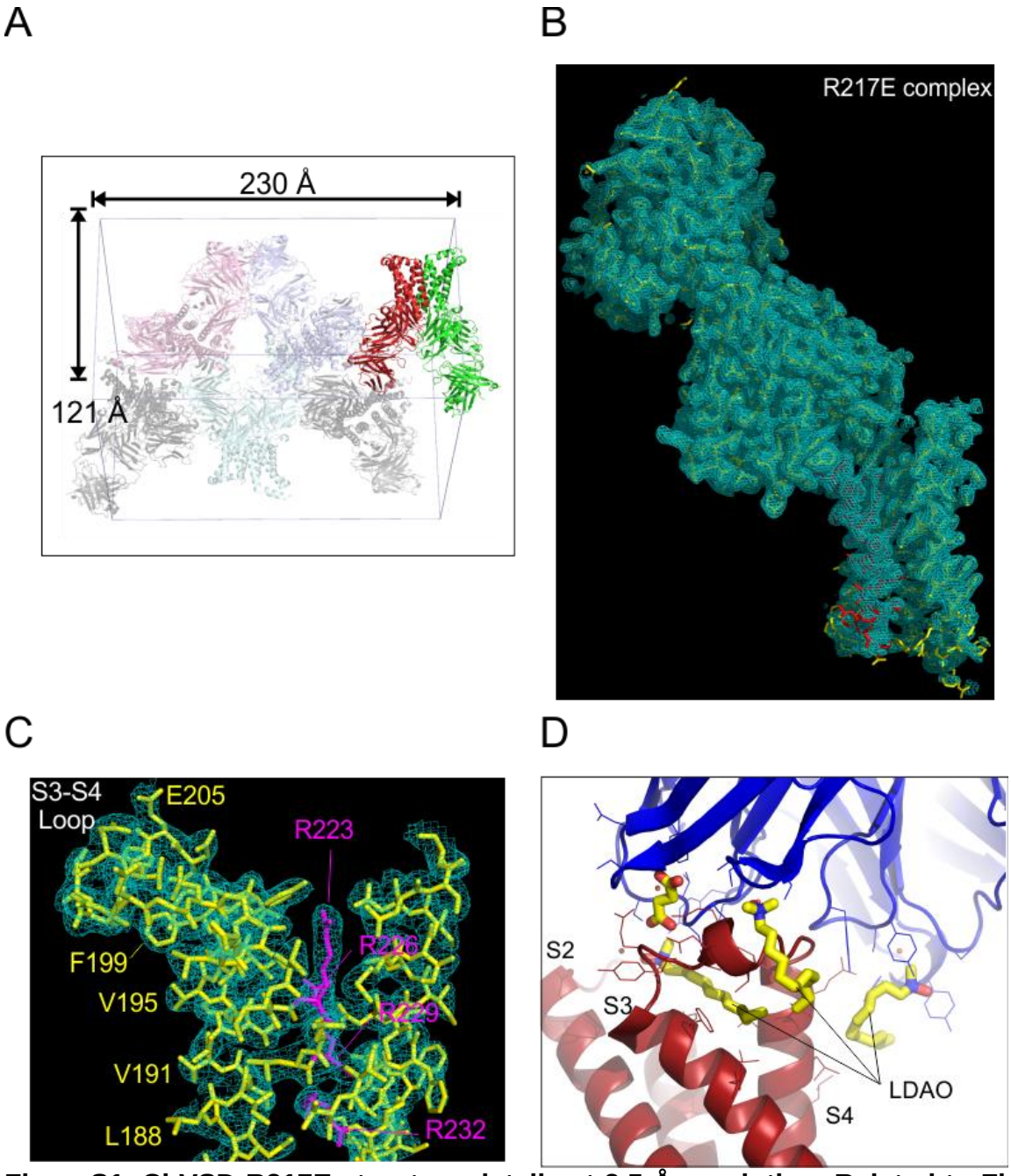

FigureS1. Ci-VSD R217E structure details at 2.5 Å resolution. Related to Figure 2. **A.** The Ci-VSD-R217E+33F12_4 crystal belongs to space group $P6_{522}$ contains 12 complexes (6 homodimers) in the unit cell. The dimer is formed with a crystallographically related symmetry partner on a screw axis. **B.** $2F_o$-F_c electron density maps (σ=1.0) of Ci-VSD-R217E complex. The S4 segment is colored in red. **C.** Close-up view of R217E structure. The side chains are well resolved at 2.5 Å resolution throughout Ci-VSD including the gating arginine residues (magenta) R223, R226, R229 and R232. **D.** Three LDAO detergent molecules and one succinic acid molecule were resolved around S3-S4 loop region of R217E structure (yellow sticks).

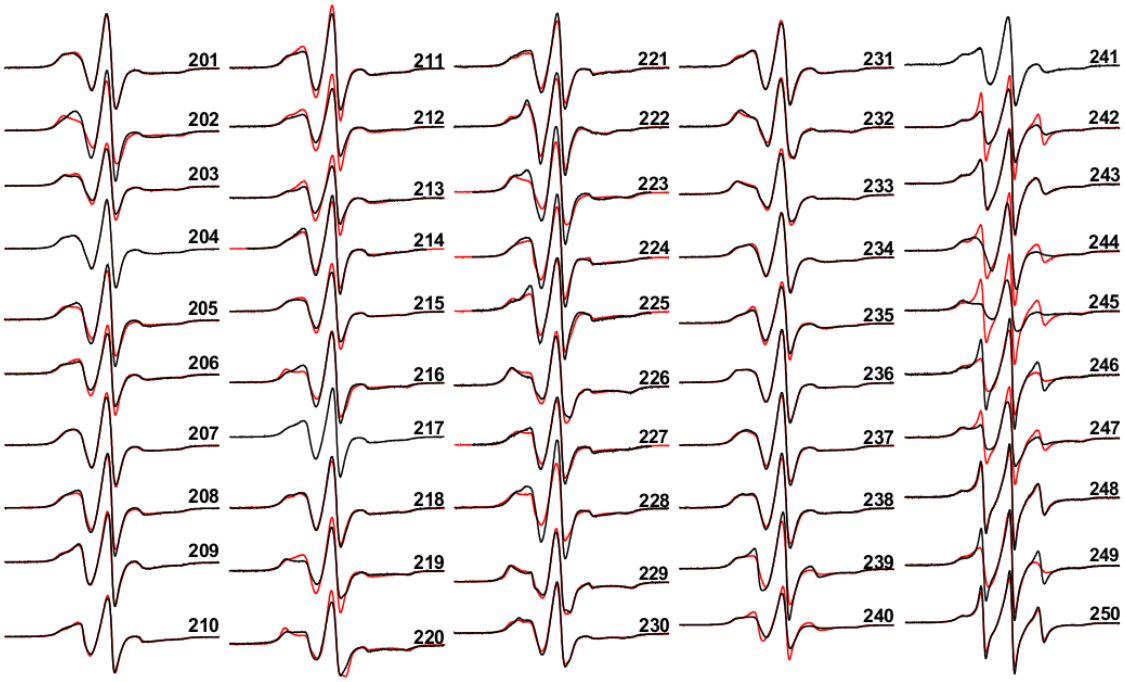

FigureS2. EPR spectra for all scanned residues. Related to Figure 3. Continuous wave EPR spectra of spin labeled single cysteine Ci-VSD-1-260 mutants on both WT (red) and R217E (black) background scanning the region 201-250. Each pair of spectra was normalized by double integration. The largest difference in spectra shape occurred at the end of the S4-phosphatse linker which is consistent with the heterogeneity of the linker from the crystal structures.

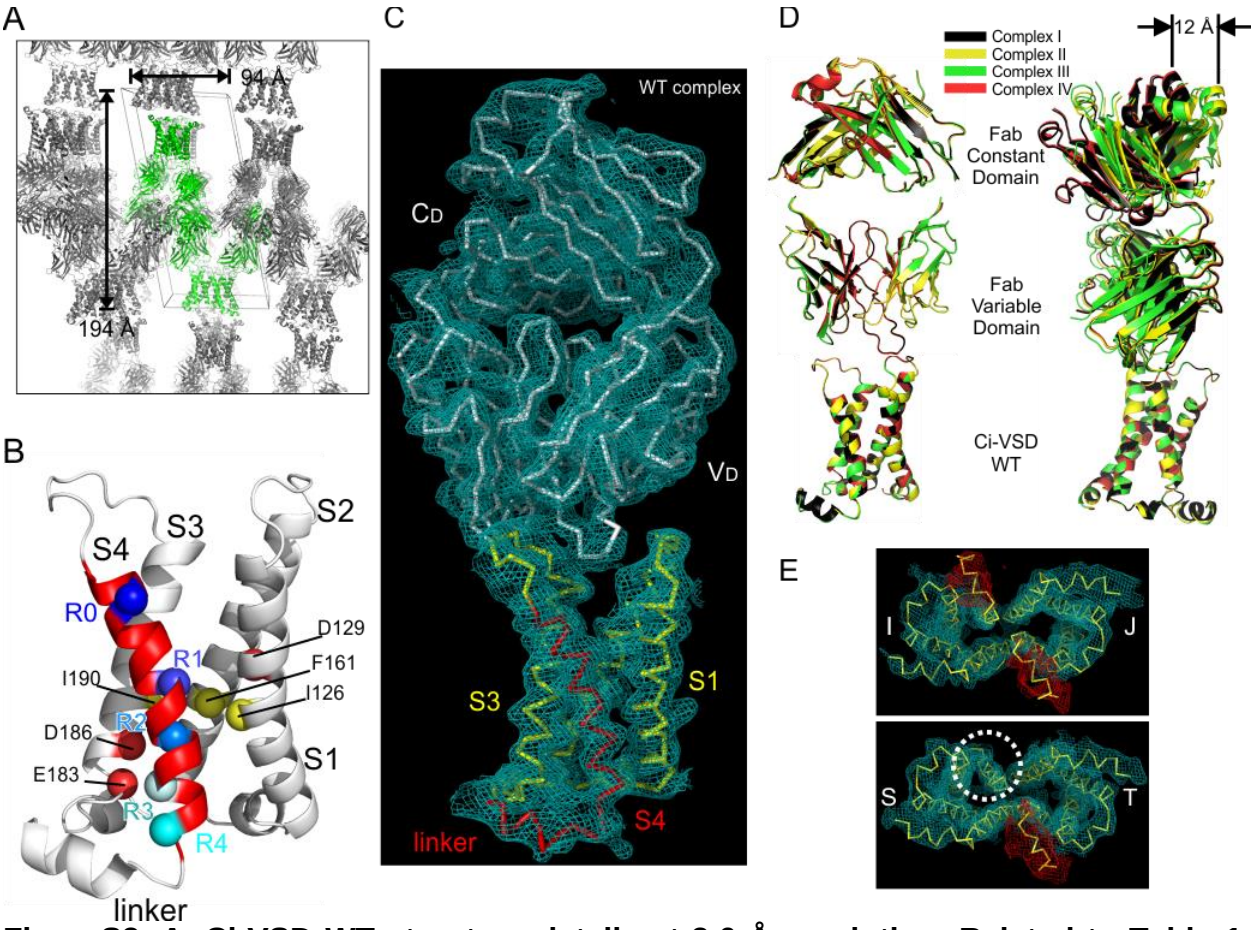

FigureS3. A. Ci-VSD WT structure details at 3.6 Å resolution. Related to Table 1. **A.** WT+39D10_18 crystal belongs to space group P1 and contains 4 complexes (2 dimers) per asymmetric unit. B. Backbone of Ci-VSD WT. **B.** Cα is shown in sphere for the S4 arginines (blue to cyan) hydrophobic gasket (yellow) and counter charges (red). **C.** $2F_o$-F_c electron density maps (σ=1.0) of one representative WT+39D10_18 complex. The S4 segment and S4-phosphatase linker were colored in red. The backbone of Ci-VSD was well resolved. **D.** Asymmetric unit of Ci-VSD-R217E+33F12_4 complex. The S4 segment is colored in red. **C.** Superposition of the four copies of the Ci-VSDWT+39D10_18 complex inside the P1 unit cell. Backbones for the three individual domains were aligned separately and overlapped with each other within the four copies (left). Dramatic differences showed up among the four complexes when they were aligned at Ci-VSD as a whole unit (right). The variation in the four variable domains is only 1~2 Å, but extends to ~12 Å among constant domains. This apparent flexibility comes from the relative position between individual structural domains, particularly between the constant and variable domains of the Fab. The individual transmembrane regions of Ci-VSD WT are shown to be essentially identical when superimposed. There is clear heterogeneity of S4-phosphtase linker in Ci-VSD-WT since it is resolved in only three out of four copies in the asymmetric unit (**E**), even though the interactions involved in S4 are the same among four copies.

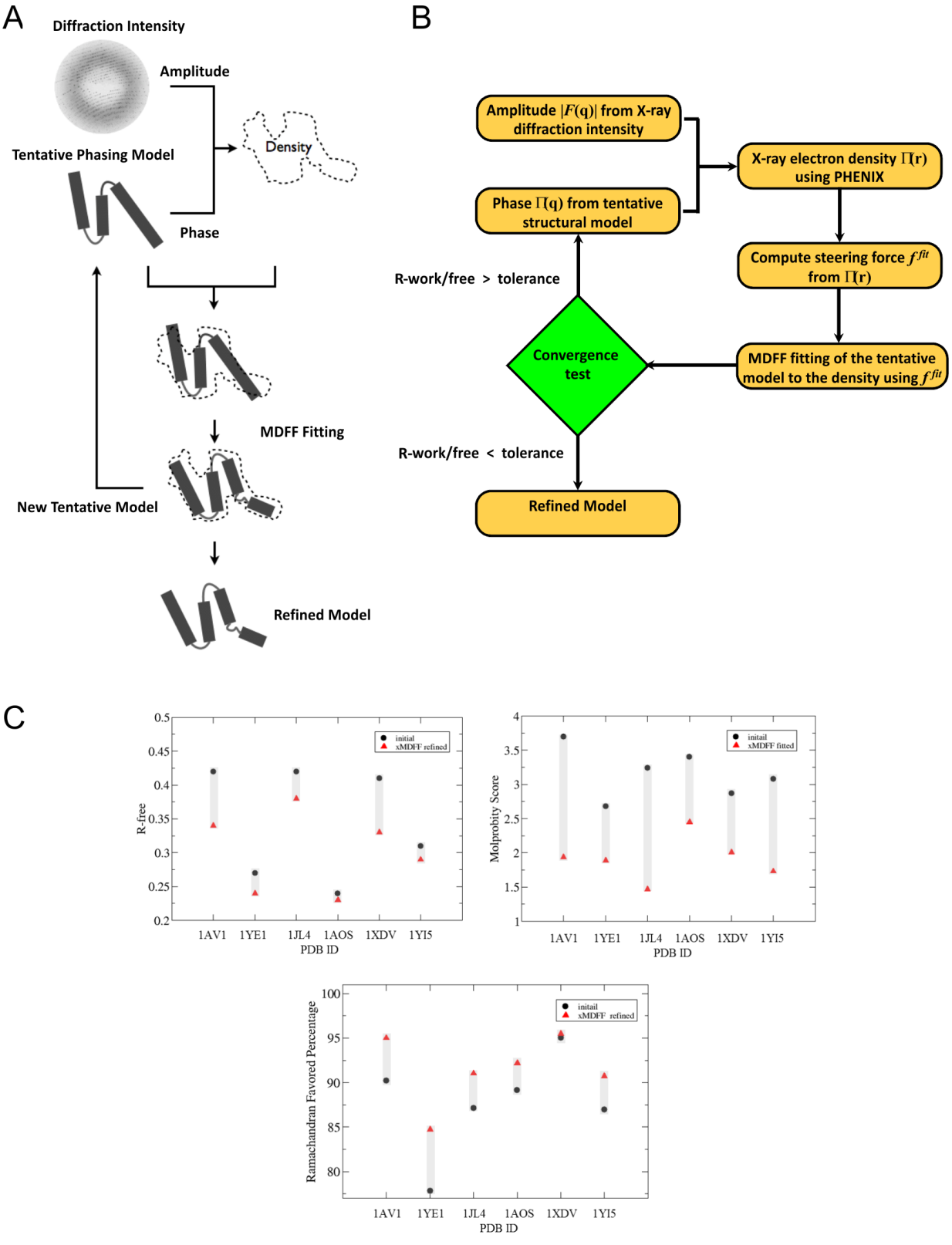
A
Diffraction Intensity
Amplitude
Density
Tentative Phasing Model
Phase
MDFF Fitting
New Tentative Model
Refined Model
B
Amplitude |F(q)| from X-ray diffraction intensity
Phase Π(q) from tentative structural model
X-ray electron density Π(r) using PHENIX
Compute steering force f^fit from Π(r)
MDFF fitting of the tentative model to the density using f^fit
Convergence test
R-work/free > tolerance
R-work/free < tolerance
Refined Model
C
R-free
initial
xMDFF refined
1AV1 1YE1 1JL4 1AOS 1XDV 1YI5
PDB ID
Molprobity Score
initail
xMDFF fitted
Ramachandran Favored Percentage
initail
xMDFF refined

Figure S4. A conceptual (A) and technical (B) workflow of xMDFF implementation, related to Figure 4. It shows the flexible fitting of an atomic model into an iteratively updated electron density map synthesized from experimental diffraction data, and the phase information obtained from the up-to-date fitted model. **C.** Improvements in R-free, MolProbity scores and percentage of Ramachandran favored conformations resulting from xMDFF refinements of six low-resolution (4-4.5Å) X-ray structures.

PDB ID	Resolution (Å)	Rotamer Outliers		Cβ Deviation		Steric Overlaps		R-work	
		initial	final	initial	final	initial	final	initial	final
1AV1	4	90	6	0	0	40.11	5.22	0.387	0.336
1YE1	4.5	39	1	14	2	17.48	10.50	0.253	0.239
1JL4	4.3	49	6	1	3	30.42	0.92	0.359	0.336
1AOS	4.2	128	32	1	1	23.60	8.65	0.201	0.211
1XDV	4.1	78	21	2	1	30.58	9.48	0.396	0.296
1Y15	4.2	192	12	4	0	8.66	4.09	0.263	0.266

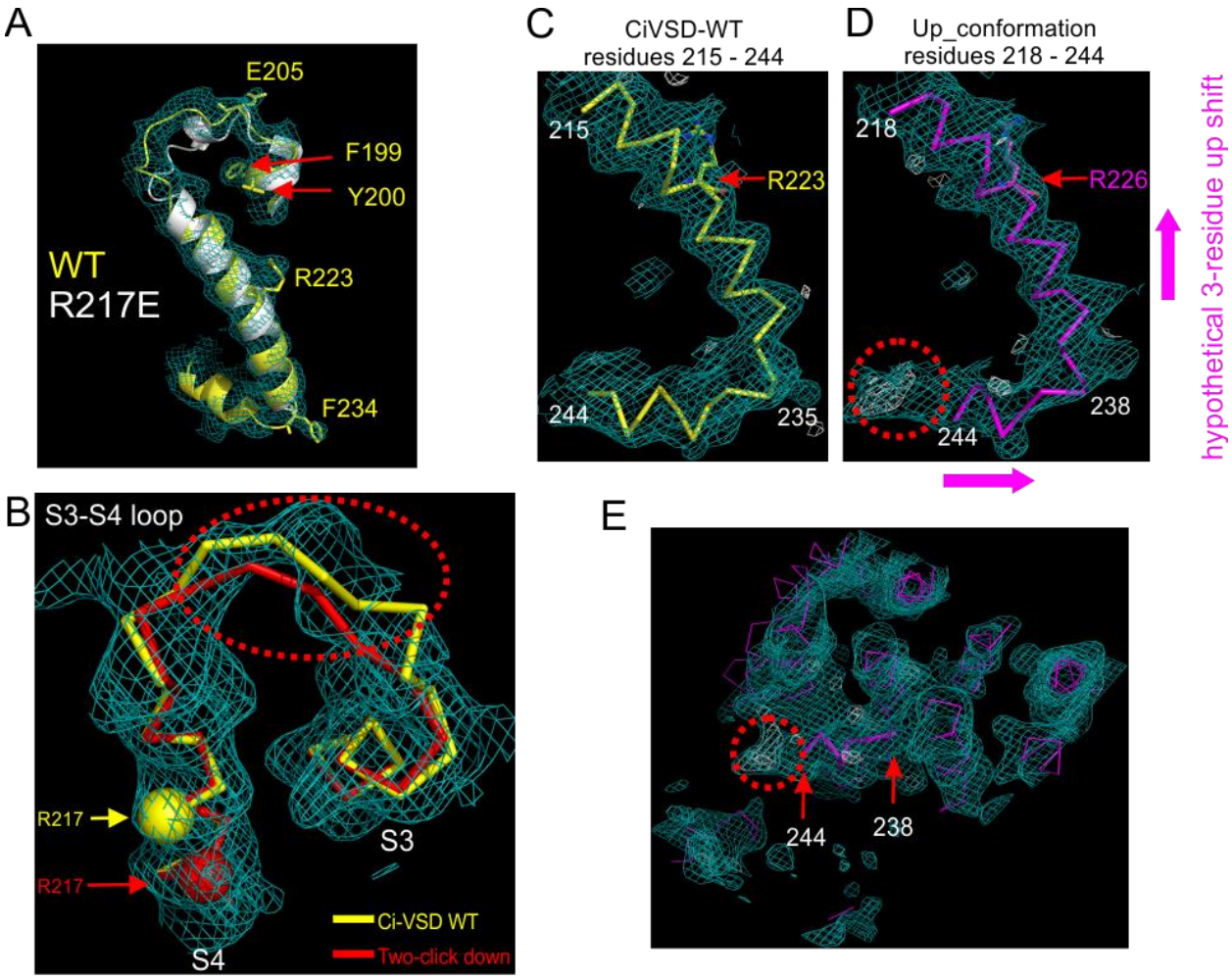

FigureS5. **Evaluation structural models with experimental density map. Related to Figure 5. A.** $2F_o$-F_c map (at σ=1.0, teal) for residues 196-244 of Ci-VSD WT (yellow ribbon) covering the top of S3, S3-S4 loop, entire S4 and S4-phosphatase linker. The R217E structure (white ribbon) with residues 196-236 was shown for comparison. The bulky residues distributed throughout the whole region were shown as F199, Y200, E205, R223 and F234. **B.** The hypothetical two-click down model (red ribbon) shift the S4 helix 3-residue downward, in reference to Ci-VSD WT model (yellow ribbon). The resulting shorter S3-S4 loop obviously deviates away from the continuous electron density map (within the red circle) and proves itself an improper model for current data. $2F_o$-F_c (at σ = 1.0, teal) and F_o-F_c (at σ = 3.0, white) maps of S4+linker for Ci-VSD-WT (**C**) and hypothetical Up-conformation model (**D**). The Up-conformation model shift S4 helix 3-residue upward which leaves unaccounted electron density after residue 244 the end of current crystallization construct for Ci-VSD, by both $2F_o$-F_c and F_o-F_c maps. The map quality around linker 238-244 in hypothetical “up-state” model was shown in (**E**) carved at 10 Å around the linker. The positive difference map (F_o-F_c) at end of the linker (white region inside red circle) is clearly above noise level.

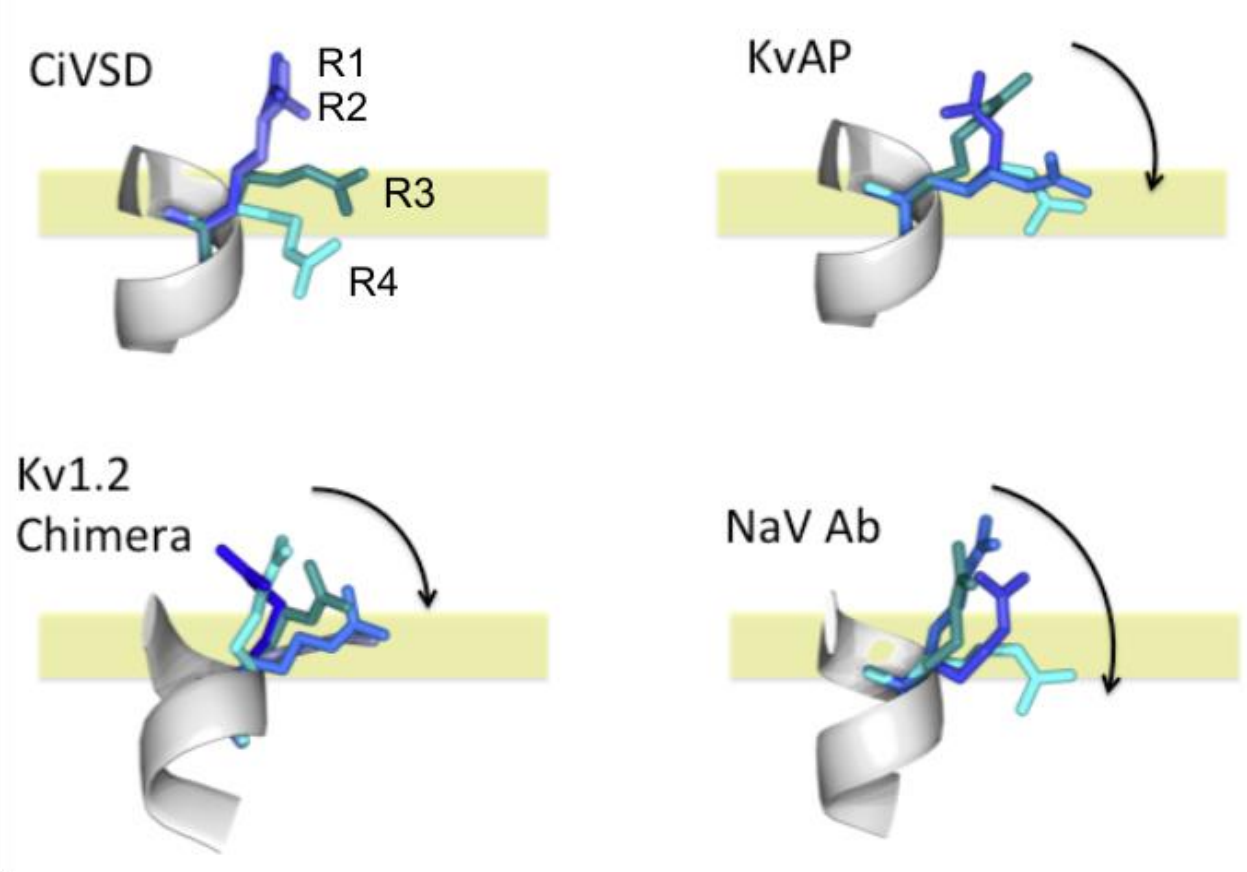

FigureS6. Rotamer orientation of gating arginines is a common motif among voltage sensors. Related to Figure 6. A large span in the relative orientation of the arginine rotamers was clearly visible if the four gating arginine residues (R223: blue, R226: lilac, R229: teal and R232: cyan) were backbone aligned in the R217E structure. R229 lies horizontally inside the hydrophobic gasket and separates the intracellular and extracellular sides electrically. R223 and R226 point straight up above the electric field, while R232 points down below the electrical field. The span of arginine rotamers were most obviously in Ci-VSD, but is also presented in other existing VSDs: KvAP, Kv1.2-2.1 chimera and NavAb (however, not in NavRh). This rotameric reorientation mechanism might be an additional contributor the total gating charge translocation in VSDs.

References

Adams, P.D., Afonine, P.V., Bunkoczi, G., Chen, V.B., Davis, I.W., Echols, N., Headd, J.J., Hung, L.W., Kapral, G.J., Grosse-Kunstleve, R.W.*, et al.* (2010). PHENIX: a comprehensive Python-based system for macromolecular structure solution. Acta Crystallogr D Biol Crystallogr *66*, 213-221.

Chen, V.B., Arendall, W.B., 3rd, Headd, J.J., Keedy, D.A., Immormino, R.M., Kapral, G.J., Murray, L.W., Richardson, J.S., and Richardson, D.C. (2010). MolProbity: all-atom structure validation for macromolecular crystallography. Acta Crystallogr D Biol Crystallogr *66*, 12-21.

DeLaBarre, B., and Brunger, A.T. (2006). Considerations for the refinement of low-resolution crystal structures. Acta Crystallogr D Biol Crystallogr *62*, 923-932.

Feller, S.E., and MacKerell, A.D. (2000). An improved empirical potential energy function for molecular simulations of phospholipids. Journal of Physical Chemistry B *104*, 7510-7515.

Humphrey, W., Dalke, A., and Schulten, K. (1996). VMD: visual molecular dynamics. J Mol Graph *14*, 33-38, 27-38.

Jo, S., Kim, T., Iyer, V.G., and Im, W. (2008). CHARMM-GUI: a web-based graphical user interface for CHARMM. J Comput Chem *29*, 1859-1865.

Jorgensen, W.L., Chandrasekhar, J., Madura, J.D., Impey, R.W., and Klein, M.L. (1983). Comparison of Simple Potential Functions for Simulating Liquid Water. Journal of Chemical Physics *79*, 926-935.

Khalili-Araghi, F., Jogini, V., Yarov-Yarovoy, V., Tajkhorshid, E., Roux, B., and Schulten, K. (2010). Calculation of the gating charge for the Kv1.2 voltage-activated potassium channel. Biophys J *98*, 2189-2198.

Klauda, J.B., Venable, R.M., Freites, J.A., O'Connor, J.W., Tobias, D.J., Mondragon-Ramirez, C., Vorobyov, I., MacKerell, A.D., Jr., and Pastor, R.W. (2010). Update of the CHARMM all-atom additive force field for lipids: validation on six lipid types. J Phys Chem B *114*, 7830-7843.

MacKerell, A.D., Bashford, D., Bellott, M., Dunbrack, R.L., Evanseck, J.D., Field, M.J., Fischer, S., Gao, J., Guo, H., Ha, S.*, et al.* (1998). All-atom empirical potential for molecular modeling and dynamics studies of proteins. Journal of Physical Chemistry B *102*, 3586-3616.

Phillips, J.C., Braun, R., Wang, W., Gumbart, J., Tajkhorshid, E., Villa, E., Chipot, C., Skeel, R.D., Kale, L., and Schulten, K. (2005). Scalable molecular dynamics with NAMD. J Comput Chem *26*, 1781-1802.

Roux, B. (2008). The membrane potential and its representation by a constant electric field in computer simulations. Biophys J *95*, 4205-4216.

Schreiner, E., Trabuco, L.G., Freddolino, P.L., and Schulten, K. (2011). Stereochemical errors and their implications for molecular dynamics simulations. BMC Bioinformatics *12*, 190.

Shaw, D.E., Deneroff, M.M., Dror, R.O., Kuskin, J.S., Larson, R.H., Salmon, J.K., Young, C., Batson, B., Bowers, K.J., Chao, J.C.*, et al.* (2008). Anton, a special-purpose machine for molecular dynamics simulation. Commun Acm *51*, 91-97.

Trabuco, L.G., Villa, E., Mitra, K., Frank, J., and Schulten, K. (2008). Flexible fitting of atomic structures into electron microscopy maps using molecular dynamics. Structure *16*, 673-683.

Trabuco, L.G., Villa, E., Schreiner, E., Harrison, C.B., and Schulten, K. (2009). Molecular dynamics flexible fitting: a practical guide to combine cryo-electron microscopy and X-ray crystallography. Methods *49*, 174-180.
Vargas, E., Bezanilla, F., and Roux, B. (2011). In search of a consensus model of the resting state of a voltage-sensing domain. Neuron *72*, 713-720.